JOURNAL OF GEOPHYSICAL RESEARCH, VOL. 111, B12S25, doi:10.1029/2006JB004529, 2006

Ferromagnetic resonance spectroscopy for assessment of magnetic anisotropy and magnetostatic interactions: A case study of mutant magnetotactic bacteria

Robert E. Kopp,[1] Cody Z. Nash,[1] Atsuko Kobayashi,[2] Benjamin P. Weiss,[3] Dennis A. Bazylinski,[4] and Joseph L. Kirschvink[1]

Received 25 May 2006; revised 28 September 2006; accepted 25 October 2006; published 28 December 2006.

[1] Ferromagnetic resonance spectroscopy (FMR) can be used to measure the effective magnetic field within a sample, including the contributions of both magnetic anisotropy and magnetostatic interactions. One particular use is in the detection of magnetite produced by magnetotactic bacteria. These bacteria produce single-domain particles with narrow size and shape distributions that are often elongated and generally arranged in chains. All of these features are detectable through FMR. Here, we examine their effects on the FMR spectra of magnetotactic bacteria strains MV-1 (which produces chains of elongate magnetite crystals), AMB-1 (which produces chains of nearly equidimensional magnetite crystals), and two novel mutants of AMB-1: mnm13 (which produces isolated, elongate crystals) and mnm18 (which produces nearly equidimensional crystals that are usually isolated). Comparison of their FMR spectra indicates that the positive magnetic anisotropy indicated by the spectra of almost all magnetotactic bacteria is a product of chain alignment and particle elongation. We also find correlations between FMR properties and magnetic measurements of coercivity and magnetostatic interactions. FMR thus provides a rapid method for assessing the magnetic properties of assemblages of particles, with applications including screening for samples likely to contain bacterial magnetofossils.

Citation: Kopp, R. E., C. Z. Nash, A. Kobayashi, B. P. Weiss, D. A. Bazylinski, and J. L. Kirschvink (2006), Ferromagnetic resonance spectroscopy for assessment of magnetic anisotropy and magnetostatic interactions: A case study of mutant magnetotactic bacteria, *J. Geophys. Res.*, *111*, B12S25, doi:10.1029/2006JB004529.

1. Introduction

[2] Ferromagnetic resonance spectroscopy (FMR), a form of electron spin resonance spectroscopy, can serve as a rapid technique for assessing the magnetic anisotropy of and magnetostatic interactions between individual particles in a polycrystalline sample. It is based upon the Zeeman effect, which is the splitting between electron spin energy levels that occurs in the presence of a magnetic field. The Zeeman effect allows a ground state electron to absorb a photon with energy equal to the splitting between the energy states. In a magnetic material, magnetic anisotropy (whether magnetocrystalline, shape, or stress induced) and interparticle interactions contribute to the energy of the particles within a sample and thereby alter the resonance energy. As a result, FMR can be used to probe these parameters [*Griscom*, 1974, 1981; *Kittel*, 1948; *Kopp et al.*, 2006; *Schlömann*, 1958; *Weiss et al.*, 2004].

[3] Techniques for measuring anisotropy and magnetostatic interactions have a number of applications in the field of rock magnetism. The example on which we will focus here is the identification of magnetite produced by magnetotactic bacteria, a topic of great interest for understanding the magnetization of sediments. Fossil magnetotactic bacteria may also serve as paleoenvironmental indicators of both strong magnetic fields and local redox gradients [*Chang and Kirschvink*, 1989; *Kirschvink and Chang*, 1984]. These bacteria are a phylogenetically diverse group that biomineralize intracellular crystals of magnetic minerals (magnetite or greigite) which orient the bacteria passively in the geomagnetic field. Natural selection has led these bacteria to optimize the magnetic moment produced for the amount of iron used. Among the traits present in magnetite produced by many magnetotactic bacteria are a narrow distribution of particle sizes within the single-domain stability field, particle elongation, and the arrangement of particles in chains [*Thomas-Keprta et al.*, 2000]. The biophysical problem of keeping strongly magnetic particles aligned in

[1]Division of Geological and Planetary Sciences, California Institute of Technology, Pasadena, California, USA.
[2]Photonics Research Institute, National Institute of Advanced Industrial Science and Technology, Osaka, Japan.
[3]Department of Earth, Atmospheric, and Planetary Sciences, Massachusetts Institute of Technology, Cambridge, Massachusetts, USA.
[4]Department of Biochemistry, Biophysics, and Molecular Biology, Iowa State University, Ames, Iowa, USA.

0148-0227/06/2006JB004529$09.00

a chain may also have driven the evolution of a variety of cytoskeletal supporting mechanisms, including an intracellular "sheath" [*Kobayashi et al.*, 2006], actin-like cytoskeletal filaments [*Scheffel et al.*, 2006] and/or direct attachments to the periplasmic membrane [*Komeili et al.*, 2006].

[4] The adaptive traits possessed by these biogenic magnetic particles at a microscopic level generate distinct magnetic properties that are identifiable with macroscopic techniques. The particles' narrow distribution within the single-domain size range is typically observed in analyses of coercivity spectra, including the measurement of the acquisition of isothermal remanent magnetization and the demagnetization of remanent magnetizations [*Chang et al.*, 1989; *Pan et al.*, 2005]. *Egli* [2004] used the unmixing of coercivity spectra to determine the biogenic contribution to lacustrine sedimentary magnetization.

[5] Anhysteretic susceptibility, which provides a qualitative measure of inverse interaction strength when comparing single-domain particles of similar volumes [*Dunlop et al.*, 1990; *Egli and Lowrie*, 2002], has also been used to distinguish bacterial magnetite chains from abiogenic magnetite [*Kopp et al.*, 2006; *Moskowitz et al.*, 1993]. Anhysteretic magnetization is acquired by the application of a small biasing field in the presence of a decaying alternating field. In the absence of thermal effects, noninteracting single-domain particles would have infinite anhysteretic susceptibility; they should become magnetized in the direction of the biasing field as soon as the alternating field decreases below their microcoercivity [*Dunlop and Özdemir*, 1997; *Egli and Lowrie*, 2002]. In fact, thermal effects cause more elongate and smaller particles to have lower anhysteretic remanent magnetization (ARM) susceptibility than less elongate or larger single-domain particles [*Egli and Lowrie*, 2002]. The shielding effects of magnetostatic interactions operating in three dimensions also lower anhysteretic susceptibility.

[6] In many strains of magnetotactic bacteria, however, linear magnetostatic interactions cause an entire chain of particles to behave in a magnetically coherent fashion [*Hanzlik et al.*, 2002; *Penninga et al.*, 1995]. Intact cells of magnetotactic bacteria therefore have low three-dimensional magnetostatic interactions and thus relatively high anhysteretic susceptibility, so high anhysteretic remanent magnetization/isothermal remanent magnetization (ARM/IRM) ratios are characteristic of the presence of magnetite chains. Collapsed magnetosome chains, with stronger three-dimensional magnetostatic interactions, have lower ARM/IRM ratios.

[7] Another test that is indicative of the presence of chains is the delta-delta test of *Moskowitz et al.* [1993], which uses the ratio of magnetization lost upon warming through the $\sim$90–120 K Verwey transition in saturated samples that have been cooled in a strong field to the magnetization lost after cooling in zero field. While previous data indicate that this test does identify chains of biogenic magnetite [*Moskowitz et al.*, 1993; *Weiss et al.*, 2004], it is susceptible to false negatives and the underlying physical mechanisms are incompletely understood [*Carter-Stiglitz et al.*, 2004].

[8] Ferromagnetic resonance spectroscopy is capable of rapidly distinguishing biogenic magnetite chains based on three traits: (1) a narrow range of particle size, shape, and arrangement, (2) chain structure, and (3) particle elongation [*Kopp et al.*, 2006; *Weiss et al.*, 2004]. Samples with narrow distributions of size, shape, and arrangement have narrow FMR peaks. Chain structure and particle elongation produce positive uniaxial anisotropy, which can be distinguished from the negative cubic magnetocrystalline anisotropy that dominates isolated, equidimensional magnetite.

[9] Bacterial mutagenesis is a central technique in molecular microbiology. By disabling regions of the genome, it probes the roles of different genes in the production of a phenotype. Our attempts to understand the molecular mechanism of magnetite biosynthesis (which will be described in a follow up paper by C. Z. Nash et al.) led us to create mutant strains of the magnetotactic bacterium *Magnetospirillum magneticum* strain AMB-1, whose wild-type creates chains of almost equidimensional cubo-octahedral crystals. Two of these mutants produce crystals that are usually isolated and are either approximately equidimensional (mutant mnm18) or elongate (mutant mnm13). We used these mutants, along with cells of wild-type AMB-1 and the magnetotactic marine vibrio MV-1, which produces chains of elongate hexaoctahedral crystals, to investigate the contributions of magnetic anisotropy and magnetostatic interactions to ferromagnetic resonance spectra. These different strains allow us for the first time to separate directly the effects of chain structure on FMR and rock magnetic properties from those of single crystal traits.

2. Methods

2.1. Mutagenesis

[10] To generate the mutants, transposon mutagenesis was performed on AMB-1 following previously described procedures [*Komeili et al.*, 2004]. Mutants were grown up on plates, and single colonies were then picked and grown up in 96-well plates in sealed jars with 2% oxygen/98% nitrogen atmospheres. After 3–5 days of growth, weakly magnetic and nonmagnetic mutants were identified by placing the plates on an array of magnets. Mutants that were not drawn toward the side of the well were subcultured for further analysis. For mutant mnm13, sequencing of genomic DNA indicated that an interruption by the introduced transposon occurred in a gene encoding for a hypothetical protein. For mnm18, sequencing indicated that the interruption occurred in a pyruvate/ferredoxin oxidoreductase gene. Time course experiments indicate that mnm18 is a growth defective mutant that takes 1–2 days longer to reach stationary phase than the wild type.

2.2. Growth Conditions and Lysis

[11] Cells of strain MV-1 were grown anaerobically with nitrous oxide as the terminal electron acceptor under heterotrophic conditions as previously described [*Dean and Bazylinski*, 1999]. Cells were harvested at early stationary phase, at a cell density of about 1.5×10^9 cells/mL, by centrifugation at 5000 $\times$ g at 4°C for 10 min and then resuspended in ice cold artificial seawater containing 20 mM Tris-HCl pH 7.0. Cells were recentrifuged and the resultant pellet of cells was frozen and shipped on dry ice to the California Institute of Technology (Caltech), where it was thawed. A fraction of the cell mass was resuspended in

Tris buffer, from which point it was subject to the same treatments as AMB-1.

[12] Two liters each of AMB-1 wild-type and mutants mnm13 and mnm18 were grown up to early stationary phase, at a cell density of about 10^8 cells/mL, using standard culture conditions [*Komeili et al.*, 2004]. The cultures were divided into thirds (A1, A2, and A3 for the wild type; B1, B2, and B3 for mnm13; C1, C2, and C3 for mnm18; V1, V2, and V3 for MV-1), spun down, and resuspended in ~5 mL 100 mM Tris buffer at pH 7. Five microliters of β-mercaptoethanol and ~250 mg of sodium dodecyl sulfate (SDS) were added to subsamples A3, B3, C3, and V3. Subsamples A2, A3, B2, B3, C2, C3, V2, and V3 were then subjected to ultrasonication with a Fisher Scientific Sonic Dismembrator 550 for about 6 min, with pulses of 0.5 s alternating with pauses of equal duration. Ultrasonication should destroy cell membranes while leaving magnetosome membranes intact. SDS treatment should destroy both cell membranes and magnetosome membranes, thereby freeing the magnetite particles from organic structures.

[13] The samples were then spun down, frozen, and freeze-dried. In a set of experiments analogous to the dilution experiments described by *Kopp et al.* [2006], V2 was diluted at ~1 part per thousand in sucrose. It was initially measured as sample V2a, then was diluted by mixing with a mortar and pestle for 4 min to form subsample V2b. Sample V3 was similarly diluted at ~1 part per thousand as sample V3a, diluted by mixing for 1 min to form sample V3b, and then mixed for four additional minutes to form sample V3c.

2.3. Electron Microscopy

[14] Specimens were dispersed on hydrophilic copper transmission electron microscopy (TEM) grids and air-dried. The grids were inserted into a beryllium TEM specimen holder for energy dispersive X-ray spectroscopy (EDS) analysis. TEM and high angle annular dark field/scanning transmission electron microscopy (HAADF/STEM) images were obtained with a Tecnai G2 F20 Twin (FEI, Holland), operating at 200 kV and equipped with Gatan energy filter GIF2001 and HAADF/STEM detecting unit. The HAADF/STEM/EDS analysis was performed by an EDX detecting unit (EDAX, Inc.). Histograms of particle size/shape distributions were made by measuring the maximum length and widths of magnetite crystals visible in the TEM images in a similar fashion to that of *Kirschvink and Lowenstam* [1979] and *Devouard et al.* [1998]. Because of the sharp decay in field strength with distance ($1/r^3$), particles were grouped into chains if they were positioned within less than one grain diameter from an adjacent crystal.

2.4. Ferromagnetic Resonance Spectra

[15] Ferromagnetic resonance spectra were acquired using an X-band Bruker ESP 300E EPR Spectrometer housed at Caltech. Except for particularly strong samples (V3a, V3b, and V3c), microwave power was set at 640 μW and spectra were integrated over three sweeps of the applied field from 0 to 600 mT. For strong samples, power was set at 64 μW and only one spectrum was acquired. To summarize spectral characteristics, we use the empirical parameters developed by *Weiss et al.* [2004] and *Kopp et al.* [2006]: g_{eff}, A, ΔB_{FWHM}, and α. The effective g factor, g_{eff}, is the g factor associated with maximum absorption which is given by $g_{\mathrm{eff}} = h\nu/\beta B_{\mathrm{eff}}$, where B_{eff} is the field value of maximum absorption. The asymmetry ratio is defined as $A = \Delta B_{\mathrm{high}}/\Delta B_{\mathrm{low}}$, where $\Delta B_{\mathrm{high}} = B_{\mathrm{high}} - B_{\mathrm{eff}}$, $\Delta B_{\mathrm{low}} = B_{\mathrm{eff}} - B_{\mathrm{low}}$, and B_{high} and B_{low} are the fields of half maximum absorption at low-field and high-field sides of the absorption peak, respectively. The full width at half maximum, ΔB_{FWHM}, is defined as $\Delta B_{\mathrm{FWHM}} = B_{\mathrm{high}} + B_{\mathrm{low}}$. Although all these parameters are derived from the integrated absorption spectrum, FMR spectra are generally displayed as derivative spectra, which magnify fine detail. The empirical parameter α, which serves as a proxy for the line width of symmetric Gaussian broadening caused by factors including heterogeneity of particle size, shape, and arrangement, is defined as $\alpha = 0.17A + 9.8 \times 10^{-4}\ \Delta B_{\mathrm{FWHM}}$/mT.

[16] The empirical parameters defined above differ from the physical parameters that control the spectral shape (g, B_{an}, K_2/K_1, and σ) and which we estimate using the models discussed in section 3. The MATLAB routines used for data analysis and fitting are available in the auxiliary material.[1]

2.5. Room Temperature Remanent Magnetization Experiments

[17] Room temperature remanent magnetization experiments were performed using a 2G Enterprises Superconducting Rock Magnetometer housing in a magnetically shielded room at Caltech and equipped with in-line coils for degaussing, DC pulsing, and applying weak DC biasing fields. Starting with an AF-demagnetized sample, anhysteretic remanent magnetization (ARM) was acquired in a 100 mT alternating field (AF) and a DC biasing field that was raised in 0.05 mT steps to 1 mT. The ARM was then removed by stepwise AF demagnetization up to 250 mT in logarithmically spaced steps (where the steps were multiples of $10^{0.1}$ mT). The sample was then imparted an isothermal remanent magnetization (IRM) by pulsing with a 100 mT field. This IRM was then removed by stepwise AF demagnetization. Finally, an IRM was imparted stepwise in logarithmically spaced steps up to 980 mT and then removed by AF demagnetization.

[18] To produce coercivity spectra from the stepwise AF and IRM curves, we took the derivative of the curves with respect to the log of the applied field and smoothed the curves with a running average. We report the following parameters: the coercivity of remanence H_{cr}, the Cisowski crossover R value, the median acquisition field of IRM ($\mathrm{MAF_{IRM}}$), the median destructive fields of IRM ($\mathrm{MDF_{IRM}}$) and ARM ($\mathrm{MDF_{ARM}}$), and the ARM ratio k_{ARM}/IRM.

[19] The parameters H_{cr} and R are determined from the IRM stepwise acquisition and demagnetization curves. H_{cr} is the field value at which the two magnetization curves cross, and R is the ratio of magnetization to saturation IRM (SIRM) at that field [*Cisowski*, 1981]. For noninteracting single-domain particles (or magnetically coherent chains of particles that do not interact with other chains), $R = 0.5$, while decreasing values indicate increasing magnetostatic

[1] Auxiliary materials are available in the HTML. doi:10.1029/2006JB004529.

interactions. The median acquisition and destructive fields are defined as the fields required to yield half of the maximum remanent magnetization, where the IRM value is taken from the stepwise IRM curve and the ARM value is taken from the ARM demagnetization curve. We report ARM susceptibility as k_{ARM}/IRM, the ARM acquired per A/m of biasing field (as measured in a biasing field of 0.1 mT (79.6 A/m) and an alternating field of 100 mT), normalized to the IRM acquired in a field of 100 mT.

2.6. Low-Temperature Rock Magnetic Experiments

[20] Low-temperature rock magnetic experiments were performed using a Quantum Design Magnetic Properties Measurement System (MPMS) housed in the Molecular Materials Resource Center of the Beckman Institute at Caltech. Following the procedure of *Moskowitz et al.* [1993], field cooled and zero-field cooled curves were acquired by cooling the sample either in a 3 T field or in zero field to 5 K, respectively, followed by pulsing with a 3 T field and then measuring the remanence magnetization during warming to room temperature in zero field. Low-temperature cycling curves when then acquired by pulsing the sample with a 3 T field at room temperature and then measuring the remanent magnetization as the sample was cooled to 10 K and then warmed to room temperature.

[21] The results of the low-temperature experiments are reported as the parameters δ_{ZFC}, δ_{FC}, and f_{LTC}. The parameters $\delta = (J_{80\mathrm{K}} - J_{150\mathrm{K}})/J_{80\mathrm{K}}$ were assessed for the zero-field-cooled and field-cooled curves, respectively, where $J_{80\mathrm{K}}$ and $J_{150\mathrm{K}}$ are the moments measured at 80 K and 150 K, respectively. A ratio $\delta_{\mathrm{FC}}/\delta_{\mathrm{ZFC}} > 2.0$ passes the Moskowitz test and is considered to be an indicator of the presence of magnetosome chains, although partial oxidation and mixing can cause intact chains to fail the test [*Moskowitz et al.*, 1993; *Weiss et al.*, 2004]. Magnetization retained through low-temperature cycling (LTC) is expressed as the memory parameter $f_{\mathrm{LTC}} = J_{\mathrm{LTC}}/J_0$, where J_0 and J_{LTC} are the room temperature magnetization measured before and after, respectively, cycling the samples to 10 K.

3. Models

[22] The models used to fit FMR spectra in this paper are a generalization of prior models [*Griscom*, 1974, 1981; *Kopp et al.*, 2006]. They derive from the resonance condition [*Smit and Beljers*, 1955, equation 7]:

$$\left(\frac{h\upsilon}{g\beta}\right)^2 = \frac{1}{M_s^2 \sin^2\vartheta}\left(\frac{\partial^2 G}{\partial\vartheta^2}\frac{\partial^2 G}{\partial\varphi^2} - \frac{\partial^2 G}{\partial\vartheta\,\partial\varphi}\right) \tag{1}$$

where $h\nu$ is the energy of the microwave photons, g is the spectroscopic g factor of an isolated particle with all anisotropy effects removed, β is the Bohr magneton (9.37×10^{-24} A m^2), M_s is the saturation magnetization, G is the free energy of the system, and ϑ and φ are the polar coordinates of the magnetization vector in its minimum energy orientation.

[23] Neglecting thermal energy, which is isotropic and therefore does not appear in equation (1), the free energy G of a system composed of noninteracting, single-domain particles can be written as a sum of the magnetostatic energy $-\mathbf{M} \bullet \mathbf{B}$ and the anisotropy energy. When the reference frame is defined such that the anisotropy axis is directed along $(\vartheta, \varphi) = (0, 0)$ as shown in Figure 1, the free energy is given by

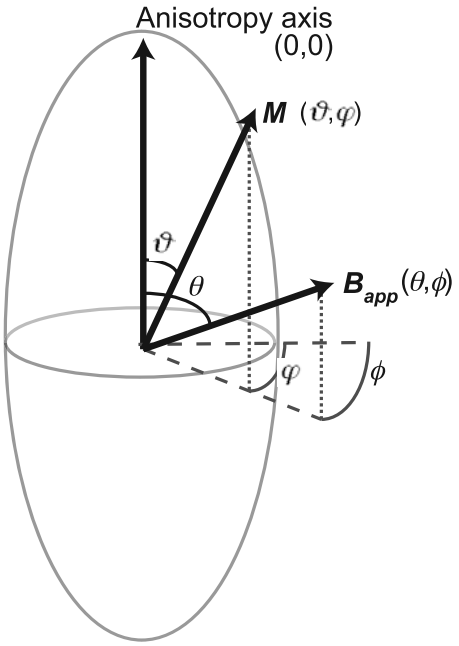

Figure 1. Angles used in the derivation of the resonance conditions. The origin of the reference frame is defined with respect to the anisotropy axis. The applied field B_{app} is oriented at azimuthal angle θ and declination ϕ. The magnetization M is oriented at azimuthal angle ϑ and declination φ.

$$G = M_s\Big\{ - B_{app}[\sin\vartheta\sin\theta\cos(\phi-\varphi) + \cos\vartheta\cos\theta]. + \frac{1}{2}B_{an}F(\vartheta,\varphi)\Big\} \tag{2}$$

where (θ, ϕ) are the polar coordinates of the experimentally applied field B_{app} with respect to the anisotropy axis, B_{an} is an effective anisotropy field, and $F(\vartheta, \varphi)$ is a geometric factor expressing the variation of the anisotropy energy as a function of the direction of the magnetization vector.

[24] B_{an} and F vary depending on the source of the anisotropy. For magnetocrystalline anisotropy, B_{an} is $2K_1/M_s$, where K_1 is the first-order anisotropy constant (generally written as K_1' for uniaxial anisotropy). For uniaxial shape anisotropy, B_{an} is $\mu_0 M_s \Delta N$, where μ_0 is the magnetic permeability of free space ($4\pi \times 10^{-7}$ N/A^2) and ΔN is the difference between the demagnetization factors $N_{\|}$ and N_{∞} parallel and perpendicular to the elongate axis. For uniaxial anisotropy, regardless of the source,

$$F(\vartheta) = \sin^2\vartheta + \frac{K_2'}{K_1'}\sin^4\vartheta \tag{3}$$

while for cubic anisotropy,

$$F(\vartheta,\varphi) = \sin^4\vartheta\sin^2\varphi\cos^2\varphi + \sin^2\vartheta\cos^2\vartheta + \frac{K_2}{K_1}\sin^4\vartheta\cos^2\vartheta\sin^2\varphi\cos^2\varphi \tag{4}$$

where K_2 is the second-order anisotropy constant (generally written as K_2' for uniaxial anisotropy) [*Dunlop and Özdemir*, 1997].

[25] By using a first-order approximation to calculate the equilibrium orientation of the magnetization vector and considering only terms that are first order in B_{an}/B_{res}, we arrive at equation A.3 of *Schlömann* [1958]:

$$\left(\frac{h\upsilon}{g\beta B_{res}}\right)^2 = 1 + \frac{B_{an}}{2B_{res}}a \tag{5}$$

where B_{res} is the applied field at which a particle in an arbitrary orientation achieves resonance and

$$a = \frac{\partial^2 F}{\partial \vartheta^2} + \frac{\partial^2 F}{\partial \varphi^2}\cdot\frac{1}{\sin^2\theta} + \frac{\partial F}{\partial \vartheta}\cot\theta \tag{6}$$

Solving the quadratic expression in equation (5) yields an expression for B_{res} as a function of orientation:

$$B_{res} = \sqrt{\left(\frac{h\upsilon}{g\beta}\right)^2 + \left(\frac{aB_{an}}{4}\right)^2} - \frac{aB_{an}}{4} \tag{7}$$

For uniaxial anisotropy,

$$a_{uniaxial} = 6\cos^2\theta - 2 + \frac{K_2'}{K_1'}\left(16\cos^2\theta\sin^2\theta - 4\sin^4\theta\right) \tag{8}$$

while for cubic anisotropy,

$$a_{cubic} = 4\left(\begin{array}{c} 1 - 5\left(\cos^2\theta\sin^2\theta + \sin^4\theta\sin^2\phi\cos^2\phi\right) \\ +\dfrac{K_2}{2K_1}\left(\begin{array}{c}\cos^2\theta\sin^2\theta + \sin^4\theta\sin^2\phi\cos^2\phi \\ -21\ \sin^4\theta\cos^2\theta\sin^2\phi\cos^2\phi\end{array}\right)\end{array}\right) \tag{9}$$

When the second-order anisotropy terms in equation (9) and the second term under the radical in equation (7) are ignored, the resonance conditions thus computed are identical to those of [*Griscom*, 1974]. When only the second term under the radical is ignored, the cubic anisotropy condition is identical to that of *Griscom* [1981], except that in equation (9) we drop the third-order anisotropy term in K_3 introduced by Griscom. The resonance conditions that we have derived are strictly correct to first order in terms of B_{an}/B_{res} for dilute powders of single-domain particles.

[26] To compute the powder absorption spectrum at B_{app}, we apply a Gaussian broadening function of line width σ and numerically integrate the spectra over all solid angles:

$$A\left(B_{app}\right) = \int_{\theta=0}^{\pi/2}\int_{\phi=0}^{2\pi}\frac{\exp\left(-\left(B_{app} - B_{res}(\theta,\phi)\right)^2/2\sigma^2\right)}{\sqrt{2\pi}\sigma}d\phi\ \sin\theta\ d\theta \tag{10}$$

The Gaussian broadening incorporates a number of physical effects, including those associated with heterogeneity of size, shape, arrangement, and composition within the sample population. To reflect the physics more accurately, the spectroscopic g factor and the anisotropy parameters ought to have population distributions associated with them individually. However, attempting to fit experimental spectra to a model that employed population distributions for each of these terms would almost always be a problem without a unique solution.

[27] We fit measured spectra to simulated spectra using nonlinear least squares fitting. For each magnetic component included, the models have four parameters that can be adjusted to fit the spectra: g, B_{an}, K_2/K_1, and σ. When appropriate, the spectra can be fit to two components, in which case K_2/K_1 is set to zero for both components in order to limit the number of additional degrees of freedom introduced.

[28] For most of the samples, we attempted fits with both cubic and uniaxial models, as well as models combining two uniaxial components, two cubic components, or a uniaxial component and a cubic component. Except when $|B_{an}| \gg \sigma$, substituting a cubic component for a uniaxial component did not significantly improve or degrade the goodness of the fit. We suspect this is because the Gaussian broadening conceals the underlying physics in a fashion that makes it difficult to discriminate between samples best fit with a cubic component and those best fit with a uniaxial component.

[29] The substitution often had only slight effects on the fitted parameters as well, but sometimes did vary the parameters outside the confidence intervals on the uniaxial fits. Because the anisotropy field expected from the cubic magnetocrystalline anisotropy of stoichiometric magnetite ($K_1 = -1.35 \times 10^4$ J/m^3, $M_s = 480$ kA/m) is about -56 mT [*Dunlop and Özdemir*, 1997], we report the fitted parameters using cubic anisotropy for components with B_{an} between approximately -56 and 0 mT. (The dominant components of samples C1 and C2 are the only components that fit this criterion.) The underlying physics in fact reflects neither purely uniaxial nor purely cubic anisotropy but a more complicated combination of approximately uniaxial shape anisotropy and cubic magnetocrystalline anisotropy, which would be reflected in a more complete form of equation (2). Some of the Gaussian broadening likely results from our simplified treatment of the anisotropy.

[30] The decision as to whether to represent a measured spectrum with a one-component spectrum or the sum of two model spectra was made heuristically, based upon the level of the improvement of fit when a second spectrum was added, how physically realistic the two spectra identified by the fitting routine are, and the size of the confidence intervals around fit parameters. In interpreting the models, it is important to remember that, if properly modeled, multiple components in a fit reflect multiple end-members mixed together (e.g., isolated particles and particles in chains, or particles in chains and particles in clumps); they do not reflect multiple aspects of the anisotropy of a single end-member.

4. Results

4.1. Electron Microscopy

[31] Consistent with the work of *Devouard et al.* [1998], our TEM images indicate that MV-1 produces chains of

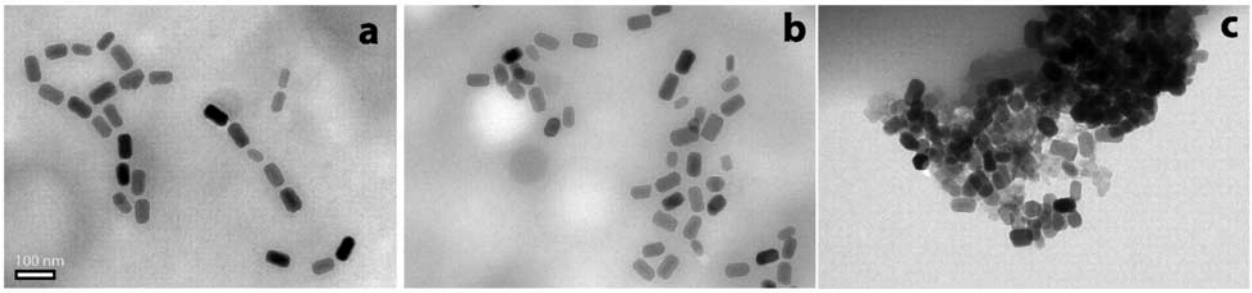

Figure 2. Transmission electron micrographs of MV-1. (a) Sample V1, untreated, (b) sample V2a, ultrasonicated, and (c) sample V3a, lysed with SDS. Scale bar is 100 nm.

magnetite crystals with a mean single-crystal length of ~75 nm and a mean length-to-width ratio of ~1.8 (Figure 2). The untreated cells of MV-1 that we measured experienced some chain collapse, perhaps due to the freezing of the sample. As can be seen in Figure 2a, some chains collapsed into zero stray field loop configurations, while in other chains some of the particles have fallen into side-by-side arrangements. About 10% of the crystals appear sufficiently separated from other crystals to be magnetically isolated. Collapse features are greatly enhanced by ultrasonication (Figure 2b). Few of the chains in the ultrasonicated sample V2 are unaffected; most are bent or interwoven with other chains. Only a small number of crystals are magnetically isolated. Treatment with SDS (sample V3) led to near complete collapse of chains into clumps (Figure 2c).

[32] There appears to be a greater tendency for chain collapse to occur in strain MV-1 than in *M. magnetotacticum* strain MS-1, a strain related to AMB-1 that produces more equidimensional particles than MV-1 [*Kobayashi et al.*, 2006]. In the case of MS-1, ultrasonication does not produce many side-by-side crystal pairs. Instead, ultrasonication of MS-1 tends to cause chains to string together in a head-to-tail fashion. The difference between the collapse styles of MV-1 and MS-1 is likely attributable to the energetic differences between elongate and equidimensional particles.

[33] Cells of wild-type AMB-1 produce magnetite particles with a mean particle length of ~35 nm and length-to-width ratio ~1.2 (Figures 3a, 3d, and 3f). In powder A1, derived from freeze-dried wild-type AMB-1, ~65% by volume of the crystals we measured were in chains of at least 2 particles and ~35% were isolated. Previous observations of whole cells of wild-type AMB-1 indicate that single cells often produce chains with segments of anywhere between 1 and 21 crystals separated by gaps. The presence of isolated crystals in the freeze-dried powder is likely due to a combination of gaps in chains produced by single cells and disaggregation during the freeze-drying process.

[34] Cells of the AMB-1 mutant mnm13 produce elongated crystals, with a mean length of ~25 nm and a mean length-to-width ratio of ~1.5 (Figures 3b, 3e, and 3h). About 90% by volume of the crystals produced by mnm13 are isolated and ~10% are in chains of 2 or more particles. Among particles with a length >25 nm, which dominate by volume and control the magnetic properties, the mean length-to-width ratio is ~1.75. Some of the bias toward greater elongation in larger crystals is likely observational; an elongate particle, viewed down the axis of elongation, appears to have a width/length ratio of 1 and a shorter length than its true length.

[35] Cells of the mutant mnm18 produce more equidimensional crystals, similar to those produced by the wild type, with a mean length of ~40 nm and a mean length-to-width ratio of ~1.2 (Figures 3c, 3f, and 3i). By volume, ~65% of the particles are isolated and ~35% are in chains. Though most of the chains consist of only two particles, they can grow significantly longer. The longest mnm18 chain we observed consisted of seven particles, which suggests that a small fraction of mnm18 cells exhibit the wild-type phenotype.

4.2. Ferromagnetic Resonance Spectroscopy

[36] Our measurements of the FMR spectra of intact MV-1 and wild-type AMB-1 agree with those of *Weiss et al.* [2004], exhibiting distinctive asymmetric spectra that are extended in the low-field direction. MV-1 has a broader spectrum than AMB-1, which reflects the greater anisotropy of its magnetite chains, generated by particle elongation as well as chain alignment (Table 1 and Figures 4 and 5). MV-1 also has three characteristic maxima in the derivative spectrum, seen in samples V1, V2a, and V2b at ~180, ~300, and ~350 mT. Our one-component model spectra are unable to reproduce this trait. Our attempts to fit these three spectra with two-component models, however, yielded disparate secondary fit components with no clear physical interpretation. This disparity suggests the values thus determined were artifacts, and we therefore report the single-component fits in Table 2. A more complete physical model capable of including multiple sources of anisotropy might explain the distinctive triple maxima of MV-1 spectra.

[37] On the basis of the demagnetization factors derived by *Osborn* [1945] and assuming that the anisotropy is dominated by uniaxial shape anisotropy, the B_{an} value of 171 mT fitted to the spectrum of intact MV-1 (sample V1) is that expected from prolate spheroids of stoichiometric magnetite (M_s = 480 kA/m) with length-to-width ratios of ~2.35. The calculated ratio is significantly larger than that observed for individual particles under TEM and therefore

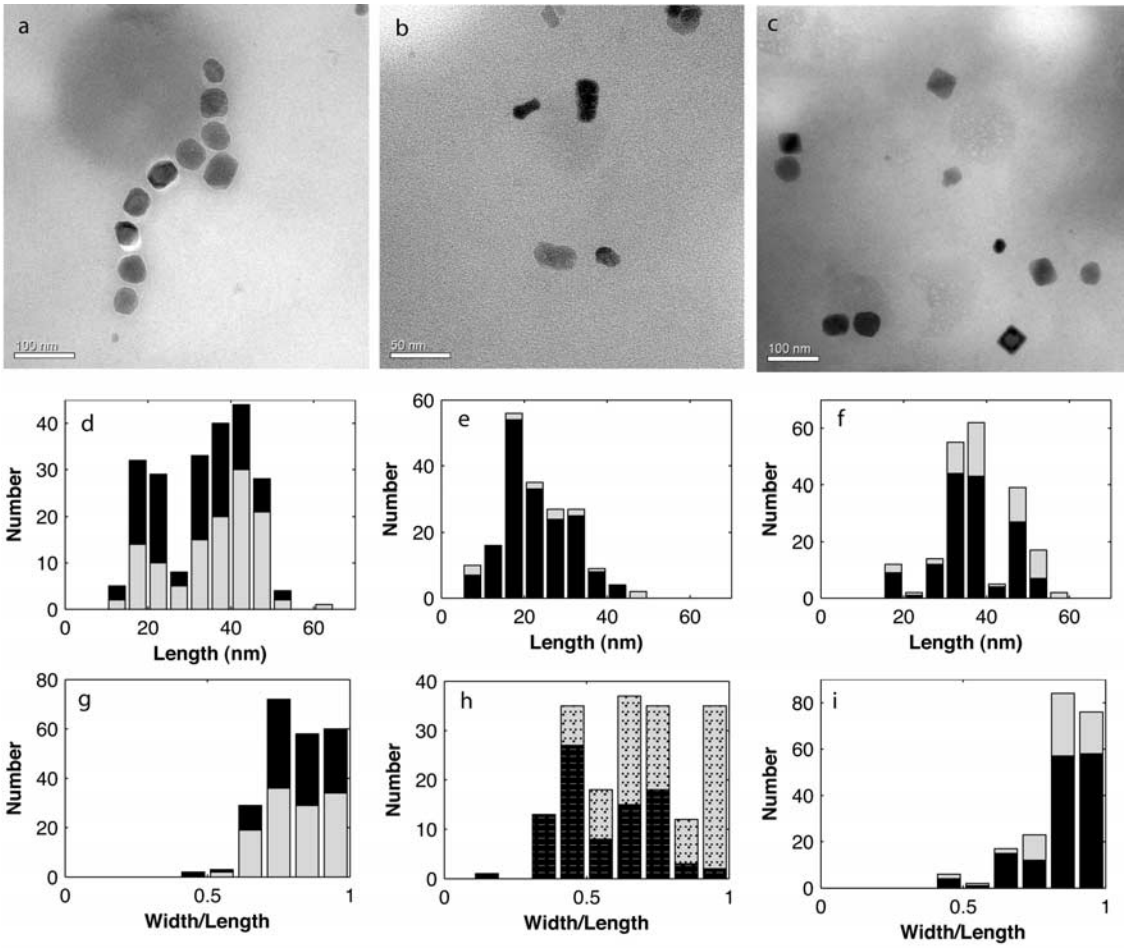

Figure 3. Transmission electron micrographs of and summary statistics for AMB-1 strains. (a–c) TEM images of freeze-dried powders of wild type (Figure 3a), mnm13 (Figure 3b), and mnm18 (Figure 3c). In Figures 3a and 3c, scale bar is 100 nm; in Figure 3b, scale bar is 50 nm. (d–f) Histograms of particle length for magnetite produced by wild type (Figure 3d), mnm13 (Figure 3e), and mnm18 (Figure 3f). (g–i) Histograms of particle width/length ratios for magnetite produced by wild type (Figure 3g), mnm13 (Figure 3h), and mnm18 (Figure 3i). In Figures 3d–3g and 3i, dark bars represent particles in chains and light bars represent isolated particles. In Figure 3h, dark bars represent particles with length $\geq$ 25 nm and light bars represent particles with length <25 nm.

likely reflects the joint contribution of particle elongation and chain structure. The large, positive B_{an} value indicates that the negative contribution of magnetocrystalline anisotropy is overwhelmed by the positive contributions of shape anisotropy and chain structure.

[38] Ultrasonication of MV-1 broadens the FMR spectrum, with ΔB_{FWHM} increasing from 127 mT in sample V1 to 219 in sample V2a. This broadening, which is reflected in the spectral fits by an increase of σ from 17 mT to 27 mT despite a slight decline in B_{an}, suggests an increase in the heterogeneity of particle arrangement without the formation of strongly interacting clumps. Although dilution (sample V2b) produces a significant increase in anhysteretic susceptibility (see discussion below), it results in little change in the FMR spectrum.

[39] In contrast, lysis of MV-1 cells with SDS produces a drastic change in the FMR spectrum, as it causes the particles to collapse into clumps. The FMR spectra of these clumps, like the FMR spectra of similarly treated AMB-1 observed by *Weiss et al.* [2004] and *Kopp et al.* [2006] and in the present work, are broad and exhibit high-field extended asymmetry reflective of a negative effective anisotropy field. The negative anisotropy may reflect the anisotropy of the surface of particle clumps or the oblateness of the clumps. Although modeling clumps with expressions derived for isolated particles is far from ideal, the fitted B_{an} value of -120 mT corresponds to that predicted for oblate spheroids with a length-to-width ratio of $\sim$0.62. [*Griscom et al.*, 1988] observed similar traits in the spectra of powders of magnetite nanoparticles exhibiting planar interactions.

[40] Subsequent dilution causes the gradual reappearance of positive anisotropy, again as in the case of AMB-1 [*Kopp et al.*, 2006]. After 1 min of dilution, the spectrum is best fit by a two-component model, with 84% of the absorption caused by a component with B_{an} of -130 mT and 16% caused by a component with B_{an} of 157 mT. The former component likely corresponds to particles in clumps, while

Table 1. Measured Ferromagnetic Resonance Parameters

Sample	Strain	Treatment	g_{eff}	A	ΔB_{FWHM}, mT	A
A1	AMB-1 wild type	untreated	2.01	0.76	87	0.21
A2	AMB-1 wild type	sonicated	2.02	0.79	84	0.22
A3	AMB-1 wild type	SDS	2.31	1.17	206	0.40
B1	AMB-1 mnm13	untreated	2.02	0.88	91	0.24
B2	AMB-1 mnm13	sonicated	2.01	0.86	95	0.24
B3	AMB-1 mnm13	SDS	2.02	0.83	107	0.25
C1	AMB-1 mnm18	untreated	2.07	1.13	80	0.27
C2	AMB-1 mnm18	sonicated	2.07	1.16	79	0.27
C3	AMB-1 mnm18	SDS	2.07	0.78	151	0.28
V1	MV-1	untreated	1.78	0.35	127	0.18
V2a	MV-1	sonicated	1.84	0.29	219	0.26
V2b	MV-1	sonicated, 4 m dilution	1.85	0.30	206	0.25
V3a	MV-1	SDS	2.58	1.77	244	0.54
V3b	MV-1	SDS, 1 m dilution	2.54	1.62	218	0.49
V3c	MV-1	SDS, 5 m dilution	1.86	0.25	208	0.25

the latter component likely corresponds to particles that are either isolated or in strings. After 5 min of dilution, the component with positive anisotropy dominates the spectrum (Figure 5).

[41] The spectrum of untreated cells of mnm13 is not markedly different from that of wild-type AMB-1 (Figure 5). Although the empirical asymmetry parameter A for mnm13 reflects a lesser degree of asymmetry than the wild type, this represents a failure of the empirical parameter; the fitted spectra reveal that mnm13 in fact has a somewhat stronger anisotropy field than the wild type, which reflects the particle elongation. The wild type has a fitted B_{an} of 69 mT, corresponding to a length-to-width ratio of ~1.35, while mnm13 has a fitted B_{an} of 91 mT, corresponding to a length-to-width ratio of ~1.50. As with MV-1, the ratio calculated for the wild type exceeds the value observed under TEM for individual particles, likely due to the effect of the chain structure in increasing B_{an}. In contrast, the ratio calculated for mnm13 corresponds to that observed under TEM.

[42] Both sonication and lysis with SDS cause a slight increase in the fitted anisotropy field of mnm13, which may reflect the formation of short strings of particles. In contrast,

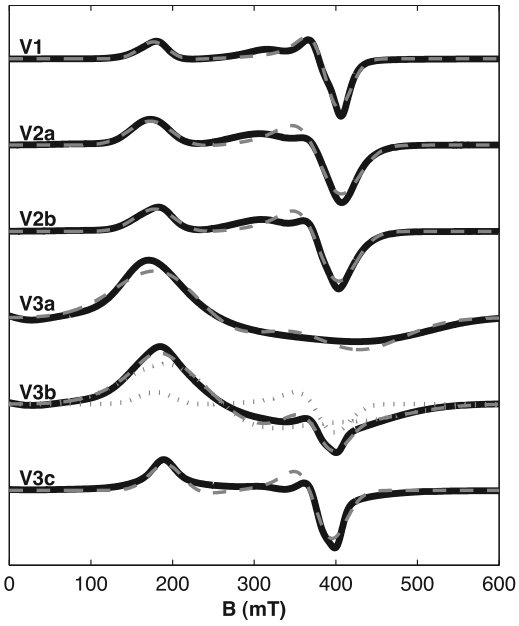

Figure 4. FMR spectra of MV-1. Solid lines show measured spectra, dashed lines show fitted spectra, and dotted lines show the spectra of the individual fit components for two-component fits.

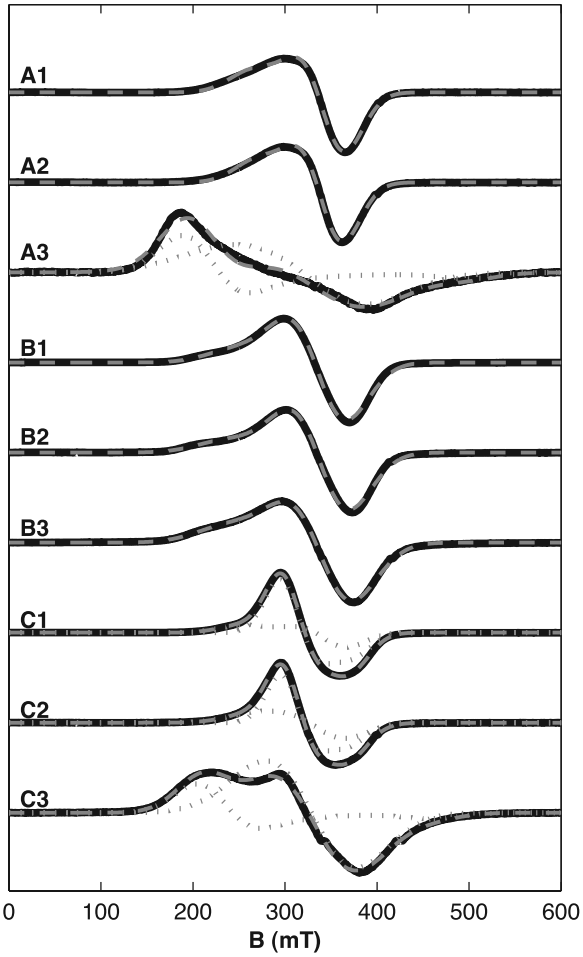

Figure 5. FMR spectra of AMB-1 wild type (A1–A3), mnm13 (B1–B3), and mnm18 (C1–C3). Solid lines show measured spectra, dashed lines show fitted spectra, and dotted lines show the spectra of the individual fit components for two-component fits.

Table 2. Ferromagnetic Resonance Spectral Fits[a]

Sample	Component Weight, %	g	B_{an}, mT	K_2/K_1	σ, mT
A1	100	2.07 ± 0.00	69.1 ± 0.8	−0.12 ± 0.01	24.2 ± 0.2
A2	100	2.07 ± 0.00	63.6 ± 0.7	−0.13 ± 0.01	23.5 ± 0.2
A3	61	2.15 ± 0.03	87.4 ± 10.1		55.5 ± 2.4
	39	2.38 ± 0.01	−171.2 ± 4.3		31.7 ± 1.5
B1	100	2.08 ± 0.00	90.9 ± 2.5	−0.32 ± 0.02	31.1 ± 0.3
B2	100	2.09 ± 0.00	104.3 ± 2.5	−0.31 ± 0.01	31.8 ± 0.2
B3	100	2.10 ± 0.00	99.7 ± 1.5	−0.23 ± 0.01	34.2 ± 0.2
C1	70	2.05 ± 0.00	−47.3 ± 0.8		19.2 ± 0.1
	30	2.12 ± 0.01	76.1 ± 1.1		22.1 ± 0.8
C2	57	2.06 ± 0.00	−43.0 ± 0.6		18.4 ± 0.2
	43	2.09 ± 0.01	64.1 ± 3.1		28.2 ± 0.6
C3	68	2.05 ± 0.01	50.2 ± 5.4		43.1 ± 0.8
	32	2.34 ± 0.01	−142.3 ± 3.3		30.4 ± 0.9
V1	100	2.21 ± 0.01	170.9 ± 2.6	−0.03 ± 0.01	17.3 ± 0.3
V2a	100	2.26 ± 0.01	164.0 ± 3.2	0.01 ± 0.01	26.7 ± 0.6
V2b	100	2.24 ± 0.01	160.4 ± 2.7	0.00 ± 0.01	24.9 ± 0.4
V3a	100	2.35 ± 0.01	−120.0 ± 2.3	0.23 ± 0.02	56.9 ± 0.8
V3b	84	2.37 ± 0.01	−129.9 ± 2.6		58.3 ± 0.9
	16	2.24 ± 0.01	157.4 ± 2.5		21.2 ± 0.7
V3c	100	2.24 ± 0.01	132.6 ± 3.4	0.08 ± 0.02	20.6 ± 0.6

[a]The dominant components of C1 and C2 are modeled using cubic anisotropy. All other components are modeled using uniaxial anisotropy.

while sonication has only slight effect on the wild type, treatment of the wild type with SDS leads to a broader spectrum that is best fit by a two-component model in which 61% of particles have positive anisotropy (B_{an} = 87 mT) and 39% have negative anisotropy (B_{an} = −171 mT). The latter component may reflect clumping. The absence of clumps in SDS-treated mnm13 suggests that the greater diluteness of the particles prevents them from clumping.

[43] The mutant mnm18 has an extremely distinctive spectrum (Figure 5). It is the only untreated magnetotactic bacterium measured so far that has $A > 1$, which reflects the negative magnetocrystalline anisotropy of isolated particles of equidimensional magnetite. It provides the best example of a spectrum that can be fitted as a mixture, as it is the mixture of two components with clear physical interpretations corresponding to TEM observations. The intact mnm18 is a mixture composed 70% of a component with negative anisotropy (B_{an} = −47 mT) and 30% of a positive anisotropy component with parameters closely resembling those of the wild type (B_{an} = 76 mT). From the FMR data, we can predict that, by volume, the sample consists 70% of isolated crystals and 30% of chains of at least 2 crystals in length. These proportions are in close agreement with the values (65% and 35%) estimated from the TEM images, which confirms the proposal by *Weiss et al.* [2004] that the uniquely asymmetric FMR spectrum of magnetotactic bacteria results primarily from the alignment of crystals in chains. We can also use this composition to unmix the isolated crystals from the other rock magnetic parameters, taking the properties of the wild type to represent those of the fraction in chains.

[44] The isolated component has a narrower Gaussian line width (σ = 20 mT) than is typical of most magnetotactic bacteria, which may reflect that lesser degree of heterogeneity possible with isolated crystals than with arrangements of crystals. The anisotropy measured for isolated crystals of mnm18 is slightly less than that expected for isolated crystals of stoichiometric magnetite dominated by cubic anisotropy, which would have B_{an} of about −56 mT. The reduced anisotropy constant ($K_1 \approx 1.1 \times 10^4$ J/m^3) may result from minor nonstochiometry (∼0.4% cation depletion) [*Kąkol and Honig*, 1989], which is consistent with the reduced Verwey transition temperature of ∼100 K observed in AMB-1 magnetite (Figure 6e) [*Muxworthy and McClellan*, 2000].

[45] Sonication of mnm18 cells leads to a slight increase in the proportion in chains, while treatment with SDS drastically alters the spectrum. SDS-treated cells of mnm18 come to resemble those of the wild-type more closely, because the sample becomes dominated by short linear strings of particles, the anisotropy of which is controlled primarily by particle arrangement. The fitted spectrum consists 68% of a component with positive anisotropy (B_{an} = 50 mT) and 32% of a component with strong negative anisotropy (B_{an} = −142 mT) comparable to those of clumps formed in SDS treatment of wild-type AMB-1 and MV-1. Thus the comparison of the unmixed components of intact and SDS-treated mnm18 provides powerful insight into the role of chain formation in controlling the magnetic properties of magnetotactic bacteria.

4.3. Isothermal Remanent Magnetization

[46] The room temperature IRM acquisition coercivity spectra for cells of wild-type AMB-1 and MV-1, regardless of treatment, agree in general shape, though not in precise parameterization, with the biogenic soft and biogenic hard components recognized by *Egli* [2004] (Figure 6a and Table 3). MV-1 has a narrow peak centered at a median field of 55 mT, while AMB-1 has a broader peak centered at 27 mT. The mutant mnm13 is slightly softer than the wild type (median field of 23 mT), which may be due to the smaller volume of mnm13 particles. The mutant mnm18 is both softer and has a broader spectrum than the other strains (median field of 16 mT). When FMR analyses and TEM observations are used to guide the unmixing of the chains and solitary particles in mnm18, the solitary particles are revealed to have a spectrum with a median coercive field of 11 mT. The drastic difference between the isolated, equidimensional

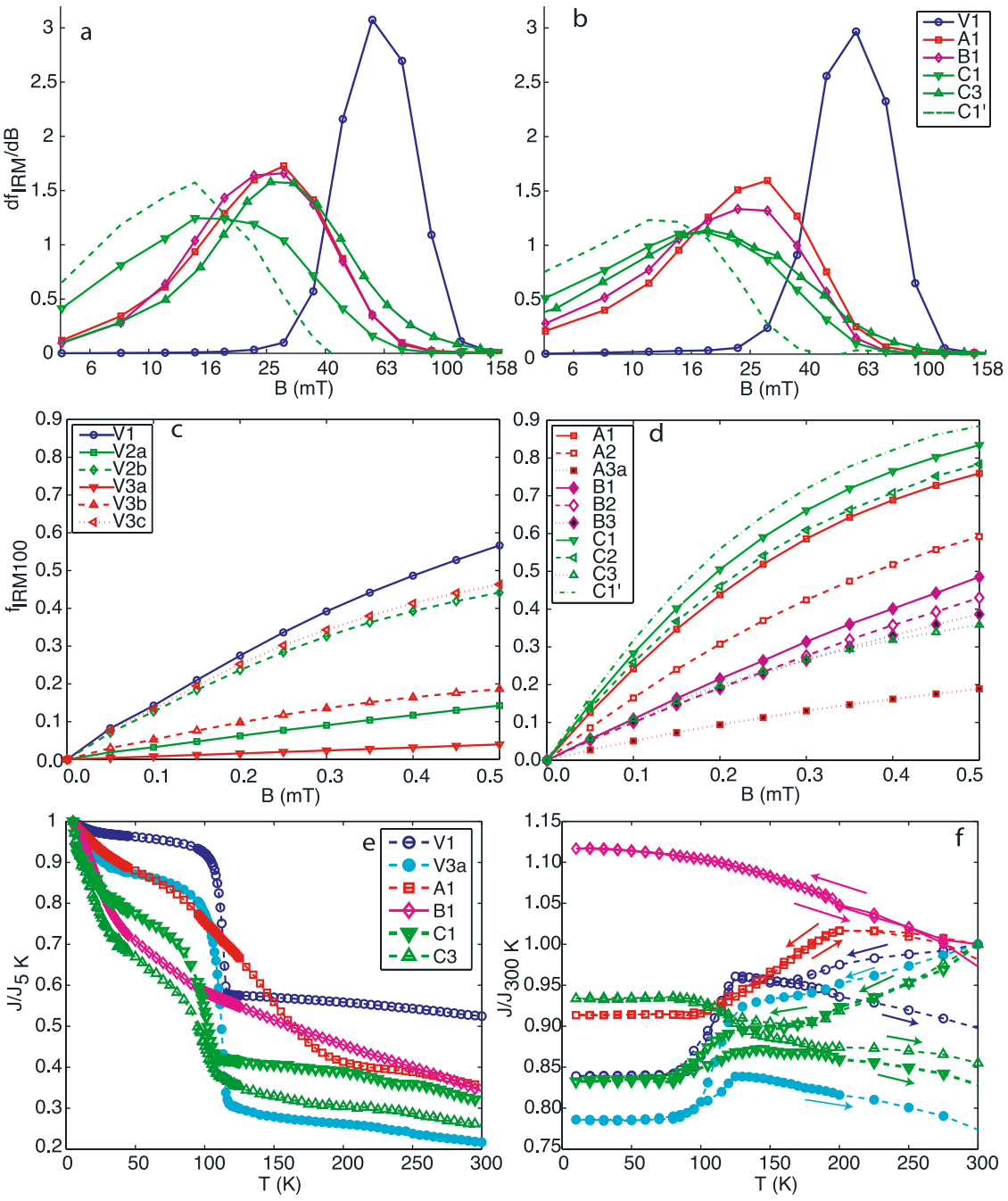

Figure 6. Rock magnetic measures of selected samples. (a–b) Coercivity spectra determined from stepwise IRM acquisition (Figure 6a) and stepwise AF demagnetization of IRM (Figure 6b). The dashed line C1' in Figure 6a, 6b, and 6d indicates the unmixed isolated particle component of C1, produced using the proportions of isolated and chain components determined from the FMR spectra to remove the chain component. (c–d) ARM acquisition curves of MV-1 (Figure 6c) and AMB-1 wild type and mutants (Figure 6d). (e–f) Low-temperature demagnetization curves. Figure 6e shows the demagnetization upon warming of a magnetization acquired by saturation at 5 K of samples cooled in a 3 T field. Magnetization values are shown normalized to the magnetization at 5 K. Figure 6f shows the demagnetization upon cooling and subsequent warming of a magnetization acquired by saturation at 300 K. Magnetization values are shown normalized to the initial room temperature magnetization.

particles produced by mnm18 and the elongate particles of mnm13, as well as the chains of equidimensional particles in the wild-type cells, highlights the role of these traits in stabilizing the magnetic moments of magnetotactic bacteria.

[47] For all samples of unlysed cells of AMB-1, both wild-type and mutant, acquisition and demagnetization curves align fairly closely (Figure 6b); Cisowski R values are all ≥ 0.42, and the median destructive field falls within 5 mT of

Table 3. Room Temperature Rock Magnetic Parameters[a]

Sample	H_{cr}, mT	R	MAF of IRM, mT	MDF of IRM, mT	MDF of ARM, mT	k_{ARM}/IRM, mm/A	Predicted Switching Field, mT
A1	24.0	0.44	26.5	21.6	22.2	2.93	30.3
A2	22.0	0.43	24.0	19.8	21.1	2.07	27.8
A3	16.6	0.29	24.1	10.2	17.4	0.64	59.8
B1	21.3	0.42	23.4	19.3	19.3	1.37	31.0
B2	23.9	0.42	26.6	22.2	22.3	1.26	35.7
B3	26.0	0.39	30.7	21.8	24.2	1.29	38.2
C1	14.5	0.47	15.7	13.8	13.7	3.55	26.7
C1'	10.7	0.44	10.6	9.9	10.5	3.99	22.3
C2	14.7	0.44	16.6	13.8	13.8	3.25	24.4
C3	21.7	0.35	26.7	16.6	21.9	1.38	39.8
V1	57.8	0.42	55.3	61.2	65.8	1.79	82.9
V2a	55.1	0.27	63.3	45.9	58.1	0.41	82.8
V2b	48.4	0.31	55.0	41.7	49.8	1.59	80.2
V3a	28.4	0.14	43.2	17.0	24.7	0.10	73.8
V3b	n.d.	n.d.	n.d.	n.d.	52.7	0.66	67.2
V3c	52.3	0.34	52.5	46.5	56.3	1.68	71.6

[a]C1′ is the unmixed end-member of C1 composed of isolated particles. Stepwise IRM curves were not measured for V3b. Predicted switching field is calculated from the FMR fit parameters as described in the text; n.d., not determined.

the median acquisition field. This is not the case for the SDS-treated mutants and both the SDS-treated and the ultrasonicated wild types, which reflects greater interparticle magnetostatic interactions in the wild types than in the mutants. Notably, the IRM acquisition curve of SDS-treated mnm18 closely resembles that of the wild type (median field of 27 mT), while the demagnetization curve remains closer to that of the untreated mnm18. As FMR data indicate the formation of linear strings of particle in the SDS-treated mnm18, the observation may suggest that IRM acquisition coercivity is more strongly affected by chain structures than is demagnetization coercivity.

4.4. Anhysteretic Remanent Magnetization

[48] The ARM acquisition curves for wild-type AMB-1 and MV-1 are consistent with previous measurements [*Moskowitz et al.*, 1993, 1988] (Figures 6c and 6d and Table 3). MV-1 has markedly lower anhysteretic susceptibility than AMB-1. Two factors likely contribute to this difference. First, as seen in the TEM images, untreated MV-1 has undergone a greater degree of chain collapse than untreated AMB-1, due to the intrinsic instability of chains of elongate particles. The increased three-dimensional magnetostatic interactions in collapsed chains serve to lower ARM susceptibility. Second, elongate particles have a higher switching field and thus lower intrinsic ARM susceptibility than more equidimensional particles of the same volume [see *Egli*, 2003, Figure 11].

[49] The pattern of variation of ARM susceptibility of lysed MV-1 shows some notable differences from parallel experiments previously reported for AMB-1 [*Kopp et al.*, 2006]. For both strains, ultrasonicated bacteria exhibit a lower susceptibility than untreated bacteria and a higher susceptibility than SDS-treated bacteria. However, whereas dilution of ultrasonicated AMB-1 produced little change in ARM susceptibility, dilution of ultrasonicated MV-1 produces significant change. Undiluted ultrasonicated MV-1 exhibits a similar susceptibility to SDS-treated MV-1 diluted for 1 min, and ultrasonicated MV-1 diluted for 4 min exhibits a similar susceptibility to SDS-treated MV-1 diluted for 5 min. The difference between the strains again likely reflects differences in collapse style between equidimensional particles and elongate particles; the strings produced by ultrasonication of AMB-1 are less likely to be reconfigured during dilution than the meshes produced by ultrasonication of MV-1.

[50] The crystals produced by mnm13 have even lower anhysteretic susceptibility than MV-1, a reflection of the combined influence of their elongation and their smaller size. In fact, their ARM susceptibility lies significantly above what would be predicted based on TEM measurements. *Egli and Lowrie* [2002] calculate that a particle with a length-to-width ratio of 1.9 and a cube root of volume of ~20 nm should have a k_{ARM}/IRM ratio of about 0.5 mm/A, whereas the measured value is 1.4 mm/A. Given the measured median destructive field, the ARM susceptibility measured would be expected for particles with a length of 45 nm and a length-to-width ratio of 1.3.

[51] The isolated particles in untreated cells of mnm18 produce one of the highest ARM susceptibilities that we have ever observed. With a k_{ARM}/IRM of 4.0 mm/A, they lie among the highest sediment values tabulated by *Egli* [2004], and above previously measured magnetotactic bacteria [*Moskowitz et al.*, 1993]. Given the similarity of the crystals produced by mnm18 to those produced by the wild type, the high k_{ARM}/IRM is likely due to the absence of magnetostatic interactions. Although they have less effect than three-dimensional interactions, even the linear interactions in wild-type AMB-1 appear to lower lower ARM susceptibility slightly.

[52] At biasing fields below 300 μT, the ARM/IRM curves of ultrasonicated mnm13 (B2), SDS-treated mnm13 (B3), and SDS-treated mnm18 (C3) are almost identical, whereas above 300 μT they diverge, with B2 > B3 > C3. The divergence may reflect the presence of a greater proportion of more strongly interacting particles (which acquire ARM in higher biasing fields) in the more severely treated samples.

4.5. Low-Temperature Magnetic Properties

[53] Regardless of treatment, the MV-1 samples have low δ_{FC}/δ_{ZFC}: the untreated and ultrasonicated samples have δ_{FC}/δ_{ZFC} of 1.4, while the SDS-treated MV-1 has δ_{FC}/δ_{ZFC} of 1.1 (Figure 6e and Table 4). On the basis of the criterion

Table 4. Low-Temperature Magnetic Parameters

Sample	δ_{ZFC}	δ_{FC}/δ_{ZFC}	f_{LTC}
A1	0.13	2.53	0.98
B1	0.17	1.07	0.97
C1	0.16	2.57	0.83
C3	0.35	1.24	0.86
V1	0.29	1.40	0.90
V2a	0.29	1.42	0.94
V3a	0.61	1.10	0.77

of *Moskowitz et al.* [1993], $\delta_{FC}/\delta_{ZFC} > 2$ indicates the presence of chains. The reason why our untreated MV-1 fails this test is unclear, although such low values have previously been observed for some fresh cultures of MV-1 (B. Moskowitz, personal communication, 2006). The low values may be related to the partial chain collapse previously described, but they stand in contrast to FMR data indicating the presence of chains. They are not a product of accidental sample oxidation; the absolute values of δ_{FC} and δ_{ZFC} are relatively large.

[54] The untreated cells of mutant mnm13 fail the Moskowitz test, with $\delta_{FC}/\delta_{ZFC} = 1.9$, consistent with the absence of chains in this sample. Inspection of its low-temperature demagnetization curves indicates that the sample's low-temperature properties are dominated by the unblocking of superparamagnetic grains, in agreement with the smaller grain size observed in the TEM images. In contrast, the untreated cells of mnm18 have $\delta_{FC}/\delta_{ZFC} = 2.6$, which slightly exceeds the wild-type value of 2.5 even though less than half of the crystals present are in chains. The unexpected result cannot be explained by nonstoichiometry, which would increase δ_{FC}/δ_{ZFC} while at the same time decreasing δ_{FC} and δ_{ZFC} [*Carter-Stiglitz et al.*, 2004]. No such drop in δ_{FC} and δ_{ZFC} is observed. Furthermore, whereas SDS treatment of mnm18 produces an FMR spectrum reflecting the presence of linear particle arrangements, it also causes δ_{FC}/δ_{ZFC} to drop to 1.2, comparable to the SDS-treated wild type [*Kopp et al.*, 2006]. The elevated δ_{FC}/δ_{ZFC} ratios of mnm18 may occur because the chain component within the sample has a higher δ_{FC}/δ_{ZFC} than the wild-type AMB-1 that we measured; previously observed δ_{FC}/δ_{ZFC} ratios for AMB-1 range as high as 5.9 [*Weiss et al.*, 2004]. Alternatively, the distinctive δ_{FC}/δ_{ZFC} ratios of magnetotactic bacteria may be due, at least in part, to same factor other than chain structure and nonstoichiometry.

[55] Consistent with prior measurements of wild-type AMB-1 [*Kopp et al.*, 2006], SDS-treated mnm18 exhibits an increase in remanence on cooling through the Verwey temperature, while intact mnm18 exhibits a decrease in remanence. In contrast, both intact and SDS-treated MV-1, like intact AMB-1, exhibit a decrease in remanence upon cooling through the Verwey transition (Figure 6f). We have no explanation for this phenomenon.

5. Discussion

[56] As measures of magnetic anisotropy and magnetostatic interaction, FMR parameters should be related to other magnetic properties that are a function of these characteristics. In so far as it possible to fit spectra well and thus obtain an accurate measurement of the anisotropy field of a sample, it is possible to use FMR spectra to estimate the switching field distribution of a sample. Neglecting thermal energy, the median coercive field of a sample is given by $B_c \approx \frac{1}{2}|B_{an}(1 + {}^{K_2}/_{K_1})|$ [*Dunlop and Özdemir*, 1997]. A plot of the calculated B_c against the median acquisition field of IRM acquisition is shown in Figure 7a.

[57] There is a good correlation between the two parameters, although the estimates derived from the FMR spectra are significantly higher than the measured values. The discrepancy is largely accounted for by the thermal

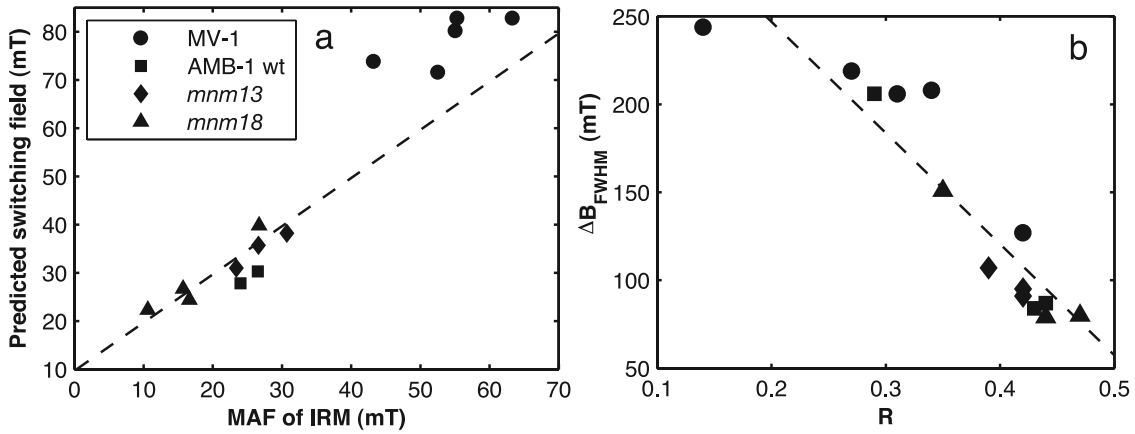

Figure 7. FMR parameters compared to rock magnetic parameters for the samples discussed in this paper. (a) Predicted switching field, determined from the weighted average of $B_c \approx \frac{1}{2}|B_{an}(1 + {}^{K_2}/_{K_1})|$ of fit components for each sample, plotted against the median acquisition field of IRM. The dashed line represents a line fitted through the points for mnm13 and mnm18 with slope fixed at 1. The line has a y intercept of 9.7 mT and a coefficient of determination $r^2 = 0.89$. (b) ΔB_{FWHM} plotted against the Cisowski R parameter, which measures magnetostatic interactions. The dashed line represents a line fitted to all samples and is given by $\Delta B_{FWHM} = 373\ mT - 632\ mT \times R$. It has a coefficient of determination $r^2 = 0.84$.

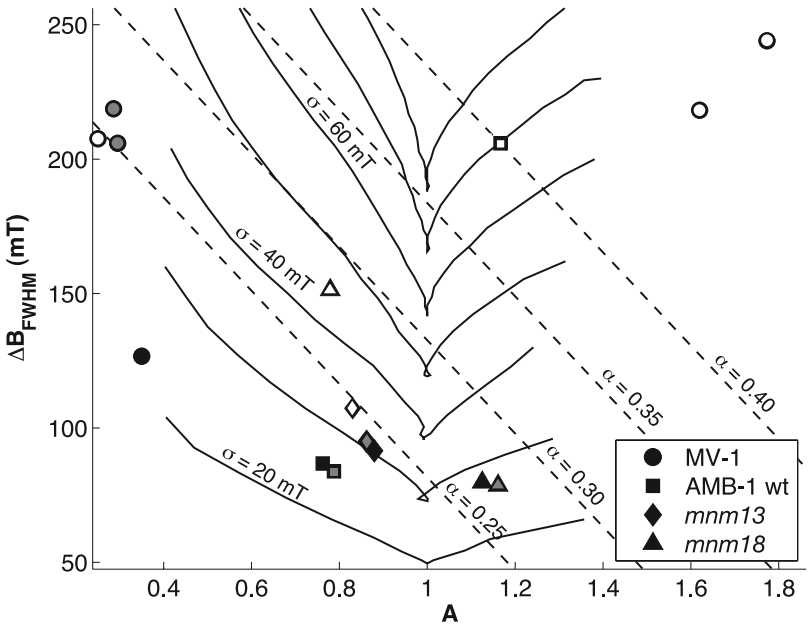

Figure 8. Plot of ΔB_{FWHM} against A for the samples discussed in this paper. Solid symbols represent untreated samples, shaded symbols represent ultrasonicated samples, and open samples represented SDS-treated samples. The dilution trend for ultrasonicated MV-1 goes slightly from the upper left to the bottom right, while the dilution trend for SDS-treated MV-1 goes from right to left. Dashed lines are contours of constant values of α. Solid lines represent simulated spectra with fixed Gaussian line width σ and variable B_{an}.

fluctuation field, which for 100 nm cubes of magnetite at room temperature is approximately $50\sqrt{B_c}$, or about 10 mT for particles with B_c = 30 mT [*Dunlop and Özdemir*, 1997]. Linear regression of the B_c values for mnm13 and mnm18, with the slope of the line fixed at 1 because of the expected theoretical relationship between B_c and MAF, yields the line B_c = MAF + 9.7 mT, with a coefficient of determination r^2 = 0.89. Removing the constraint on the slope does not significantly improve the fit. The y intercept thus calculated is in agreement with the expected thermal fluctuation field.

[58] Cells of mutant AMB-1 and intact cells of wild-type AMB-1 have B_c close to those predicted from the regression line, but SDS-treated cells of AMB-1 and all MV-1 samples fall well off the line. This difference may be due to a combination of imperfect fitting of the FMR spectra and the presence of additional factors not treated in the simple physical model used to predict B_c.

[59] There is no single parameter that perfectly reflects interaction field strength [*Dunlop et al.*, 1990], but the crossover R value of *Cisowski* [1981] is commonly used. The strength of three-dimensional magnetostatic interactions affects two parameters employed in modeling FMR spectra: the anisotropy field B_{an} and the Gaussian line width σ. Local anisotropy in magnetostatic interactions, such as that which occurs on the surface of a clump of particles, alters the anisotropy field, while the heterogeneity of local magnetic environments produced by interactions results in an increase in Gaussian line width. Other factors also contribute to both these terms, however, so neither provides a good measure of interaction field strength. The empirical line width parameter ΔB_{FWHM} appears to provide a better measure, as it correlates reasonably well with the Cisowski R parameter (Figure 7b). Linear regression yields the relationship ΔB_{FWHM} = 373 mT − 632 mT × R, with a coefficient of determination r^2 = 0.84. When present, strong three-dimensional interactions overwhelm other factors controlling ΔB_{FWHM}, such as single-particle anisotropy and linear interactions.

[60] The bacterial samples measured in this work continue to support the use of the empirical discriminant factor α [*Kopp et al.*, 2006] to distinguish biogenic magnetite chains (Figure 8). Of all the intact cells of magnetotactic bacteria we measured, only those of the mutant mnm18 have $\alpha > 0.24$. This exception arises because mnm18 has $A > 1$ and, while α serves as a proxy for Gaussian line width σ when σ is around 30 mT and $A < 1$, it does not when $A > 1$, as can be seen from the α contours plotted on Figure 8. As can be seen from the contours on Figure 8, mnm18 falls within the domain of intact magnetotactic bacterial cells when σ values of synthetic spectra are used to delineate boundaries.

[61] Ultrasonication in general results in a slight increase in α, which confirms prior results [*Kopp et al.*, 2006]. SDS treatments of the wild-type cells of both MV-1 and AMB-1 result in drastic shifts in α as highly interacting clumps come to dominate the sample. The increase in α that occurs with SDS treatment of cells of the AMB-1 mutants, in which the magnetite is more dilute, is present but subtle. SDS-treated cells of both wild-type strains, when diluted by mixing for 5 min, experience a significant reduction in α to values characteristic of the domain previously identified as being the magnetofossil domain, namely $\alpha < 0.30$ [*Kopp et al.*, 2006].

[62] In agreement with *Kopp et al.* [2006] and *Weiss et al.* [2004], these data support the use of ferromagnetic reso-

nance spectroscopy as a technique for identifying potential magnetofossils in the sedimentary record. Because it can provide a rapid way of estimating the biogenic contribution to sedimentary magnetism, FMR has the potential to be a highly useful tool for environmental magnetism and magnetic paleobiology.

6. Conclusion

[63] We have generated mutant strains of magnetotactic bacteria that allow us to start to untangle the contributions of chain arrangement and particle elongation to the ferromagnetic resonance and rock magnetic properties of magnetotactic bacteria. The four strains we have analyzed represent all four possible combinations of chain and solitary particles, and elongate and equidimensional particles. In addition, the SDS-treated cells of mnm18 allow us to investigate the changes that occur as solitary equidimensional particles assemble into linear structures. Our findings indicate that ferromagnetic resonance spectroscopy provides an effective technique for estimating the switching field distribution and interaction effects within a sample and continue to support the use of ferromagnetic resonance spectroscopy as a way of identifying magnetotactic bacteria and magnetofossils. Since it takes only a few minutes to acquire a FMR spectrum, which is significantly faster than most rock magnetic techniques being used for similar purposes, we hope that our work will spur the broader adoption of ferromagnetic resonance spectroscopy by the rock magnetic community.

Notation

FMR: Empirical Parameters

A asymmetry ratio = $\Delta B_{\text{high}}/\Delta B_{\text{low}}$.

B_{eff} applied field at peak of integrated absorption spectrum, mT.

ΔB_{FWHM} full width at half maximum, $\Delta B_{\text{high}} + \Delta B_{\text{low}}$.

ΔB_{high} (ΔB_{low}) half width at half maximum of integrated spectrum on high-field (low-field) side of peak, mT.

g_{eff} g value at absorption peak, $h\nu/\beta B_{\text{eff}}$.

α empirical discriminant factor, $0.17\ A + 9.8 \times 10^{-4}\ \text{mT}^{-1}\ \Delta B_{\text{FWHM}}$.

FMR: Empirical Parameters

B_{an} effective anisotropy field: $2K_1/M$ for magnetocrystalline anisotropy, $\mu_0 M_s \Delta N$ for shape anisotropy.

g true spectroscopic g-factor (equivalent to g_{eff} when $B_{an} = 0$).

K_2/K_1 ratio of second-order and first-order anisotropy constants.

σ standard deviation of Gaussian broadening function.

Rock Magnetic Parameters

H_{cr} coercivity of remanence, determined here from intersection point of IRM acquisition and demagnetization curves, mT.

f_{LTC} fraction of room temperature SIRM retained after cycling to low temperature and back.

k_{ARM}/IRM ARM susceptibility normalized to IRM (measured here with 0.1 mT ARM biasing field, 100 mT ARM alternating field, and 100 mT IRM pulse field), mm/A.

MAF (MDF) median acquisition (destructive) fields, at which half of a total remanence is acquired (destroyed), mT.

R Cisowski R parameter, reflecting magnetostatic interactions: fraction of IRM remaining at H_{cr}.

δ_{FC} (δ_{ZFC}) $(J_{80\text{K}} - J_{150\text{K}})/J_{80\text{K}}$ for field-cooled (zero-field-cooled) low-temperature SIRM thermal demagnetization curves.

[64] **Acknowledgments.** We thank Angelo Di Bilio for assistance with the EPR spectrometer, Arash Komeili for assistance with the mutagenesis, and Mike Jackson, David Griscom, and an anonymous reviewer for helpful comments. The Beckman Institute provided support for the use of the MPMS. R.E.K., J.L.K., and C.Z.N. would like to thank the Agouron Institute, the Moore Foundation, and the NASA Astrobiology Science and Technology Instrument Development program for support. A.K. was partially supported by funds from a New Energy and Industrial Technology Development Organization fellowship. D.A.B. was supported by U.S. National Science Foundation grant EAR-0311950. B.P.W. thanks the NASA Mars Fundamental Research and NSF Geophysics Programs.

References

Carter-Stiglitz, B., B. Moskowitz, and M. Jackson (2004), More on the low-temperature magnetism of stable single domain magnetite: Reversibility and non-stoichiometry, *Geophys. Res. Lett.*, *31*, L06606, doi:10.1029/2003GL019155.

Chang, S. B. R., and J. L. Kirschvink (1989), Magnetofossils, the magnetization of sediments, and the evolution of magnetite biomineralization, *Annu. Rev. Earth Planet. Sci.*, *17*, 169–195.

Chang, S. B. R., et al. (1989), Biogenic magnetite in stromatolites. 2. Occurrence in ancient sedimentary environments, *Precambrian Res.*, *43*, 305–315.

Cisowski, S. (1981), Interacting vs. non-interacting single-domain behavior in natural and synthetic samples, *Phys. Earth Planet. Inter.*, *26*, 56–62.

Dean, A. J., and D. A. Bazylinski (1999), Genome analysis of several marine, magnetotactic bacterial strains by pulsed-field gel electrophoresis, *Curr. Microbiol.*, *39*, 219–225.

Devouard, B., et al. (1998), Magnetite from magnetotactic bacteria: Size distributions and twinning, *Am. Mineral.*, *83*, 1387–1398.

Dunlop, D. J., and Ö. Özdemir (1997), *Rock Magnetism: Fundamentals and Frontiers*, 573 pp., Cambridge University Press, New York.

Dunlop, D. J., et al. (1990), Preisach diagrams and anhysteresis: Do they measure interactions, *Phys. Earth Planet. Inter.*, *65*, 62–77.

Egli, R. (2003), Analysis of the field dependence of remanent magnetization curves, *J. Geophys. Res.*, *108*(B2), 2081, doi:10.1029/2002JB002023.

Egli, R. (2004), Characterization of individual rock magnetic components by analysis of remanence curves, 1. Unmixing natural sediments, *Studia Geophys. Geod.*, *48*, 391–446.

Egli, R., and W. Lowrie (2002), Anhysteretic remanent magnetization of fine magnetic particles, *J. Geophys. Res.*, *107*(B10), 2209, doi:10.1029/2001JB000671.

Griscom, D. L. (1974), Ferromagnetic resonance spectra of lunar fines: Some implications of line shape analysis, *Geochim. Cosmochim. Acta*, *38*, 1509–1519.

Griscom, D. L. (1981), Ferromagnetic resonance condition and powder pattern analysis for dilute, spherical, single-domain particles of cubic crystal structure, *J. Magn. Reson.*, *45*, 81–87.

Griscom, D. L., et al. (1988), Ferromagnetic-resonance studies of iron-implanted silica, *Nucl. Instrum. Methods Phys. Res., Sect. B*, *32*, 272–278.

Hanzlik, M., et al. (2002), Pulsed-field-remanence measurements on individual magnetotactic bacteria, *J. Magn. Magn. Mater.*, *248*, 258–267.

Kąkol, Z., and J. M. Honig (1989), Influence of deviations from ideal stoichiometry on the anisotropy parameters of magnetite $Fe_{3(1-\delta)}O_4$, *Phys. Rev. B*, *40*, 9090–9097.

Kirschvink, J. L., and S. B. R. Chang (1984), Ultrafine-grained magnetite in deep-sea sediments: Possible bacterial magnetofossils, *Geology*, *12*, 559–562.

Kirschvink, J. L., and H. A. Lowenstam (1979), Mineralization and magnetization of chiton teeth: Paleomagnetic, Sedimentologic, and biologic implications of organic magnetite, *Earth Planet. Sci. Lett.*, *44*, 193–204.

Kittel, C. (1948), On the theory of ferromagnetic resonance absorption, *Phys. Rev.*, *73*, 155–161.

Kobayashi, A., et al. (2006), Experimental observation of magnetosome chain collapse in magnetotactic bacteria: Sedimentological, paleomagnetic, and evolutionary implications, *Earth Planet. Sci. Lett.*, *245*, 538–550.

Komeili, A., et al. (2004), Magnetosome vesicles are present before magnetite formation, and MamA is required for their activation, *Proc. Natl. Acad. Sci. U.S.A.*, *101*, 3839–3844.

Komeili, A., et al. (2006), Magnetosomes are cell membrane invaginations organized by the actin-like protein MamK, *Science*, *311*, 242–245.

Kopp, R. E., et al. (2006), Chains, clumps, and strings: Magnetofossil taphonomy with ferromagnetic resonance spectroscopy, *Earth Planet. Sci. Lett.*, 10–25.

Moskowitz, B. M., et al. (1988), Magnetic properties of magnetotactic bacteria, *J. Magn. Magn. Mater.*, *73*, 273–288.

Moskowitz, B. M., et al. (1993), Rock magnetic criteria for the detection of biogenic magnetite, *Earth Planet. Sci. Lett.*, *120*, 283–300.

Muxworthy, A. R., and E. McClellan (2000), Review of the low-temperature magnetic properties of magnetite from a rock magnetic perspective, *Geophys. J. Int.*, *140*, 101–114.

Osborn, J. A. (1945), Demagnetizing factors of the general ellipsoid, *Phys. Rev.*, *67*, 351–357.

Pan, Y. X., et al. (2005), Rock magnetic properties of uncultured magnetotactic bacteria, *Earth Planet. Sci. Lett.*, *237*, 311–325.

Penninga, I., et al. (1995), Remanence measurements on individual magnetotactic bacteria using a pulsed magnetic-field, *J. Magn. Magn. Mater.*, *149*, 279–286.

Scheffel, A., et al. (2006), An acidic protein aligns magnetosomes along a filamentous structure in magnetotactic bacteria, *Nature*, *440*, 110–114.

Schlömann, E. (1958), Ferromagnetic resonance in polycrystal ferrites with large anisotropy: General theory and application to cubic materials with a negative anisotropy constant, *J. Phys. Chem. Solids*, *6*, 257–266.

Smit, J., and H. G. Beljers (1955), Ferromagnetic resonance absorption in $BaFe1_2O_{19}$, a highly anisotropic crystal, *Philips Res. Rep.*, *10*, 113–130.

Thomas-Keprta, K. L. (2000), Elongated prismatic magnetite crystals in ALH84001 carbonate globules: Potential Martian magnetofossils, *Geochim. Cosmochim. Acta*, *64*, 4049–4081.

Weiss, B. P., et al. (2004), Ferromagnetic resonance and low temperature magnetic tests for biogenic magnetite, *Earth Planet. Sci. Lett.*, *224*, 73–89.

D. A. Bazylinski, Department of Biochemistry, Biophysics, and Molecular Biology, Iowa State University, Ames, IA 50011, USA.

J. L. Kirschvink, R. E. Kopp, and C. Z. Nash, Division of Geological and Planetary Sciences, California Institute of Technology, 170-25, Pasadena, CA 91125, USA. (rkopp@caltech.edu)

A. Kobayashi, Photonics Research Institute, National Institute of Advanced Industrial Science and Technology, 1-8-31 Midorigaoka, Ikeda, Osaka 563-8577, Japan.

B. P. Weiss, Department of Earth, Atmospheric, and Planetary Sciences, Massachusetts Institute of Technology, Cambridge, MA 02139, USA.